

# Quantitative Unmixing in Photoswitching Optoacoustic Tomography

YAN LIU,<sup>1</sup> JONATHAN CHUAH,<sup>1</sup> ANDRE C. STIEL,<sup>2,3</sup> MICHAEL UNSER,<sup>1,\*</sup> AND JONATHAN DONG<sup>1</sup>

<sup>1</sup>*Biomedical Imaging Group, École polytechnique fédérale de Lausanne, Station 17, 1015 Lausanne, Switzerland*

<sup>2</sup>*Institute of Biological and Medical Imaging, Helmholtz Zentrum München, Neuherberg, Germany*

<sup>3</sup>*Faculty of Biology and Pre-Clinical Medicine, University of Regensburg, Regensburg, Germany*  
*\*michael.unser@epfl.ch*

**Abstract:** Optoacoustic (OA) imaging combined with reversibly photoswitchable proteins has emerged as a promising technology for the high-sensitivity and multiplexed imaging of cells in live tissues in preclinical research. Through carefully-designed illumination schedules of ON and OFF laser pulses, the resulting OA signal is a multiplex of different reporter species and the background. By exploiting their distinct inherent photo-physical properties which govern the rate of switching, one can recover the concentration maps of protein reporters from the temporally entangled OA images. In this paper, we propose a quantitative unmixing approach in the form of a regularized inversion algorithm based on a mathematical model of the temporal decay of the signal measuring the underlying protein reporters. We validate three types of reporters on simulated and experimental datasets and show successful unmixing results.

## 1. Introduction

Optoacoustic tomography (OAT), also known as photoacoustic tomography, is a powerful and versatile imaging technology to perform multiscale imaging from organelles to whole-body small animals at penetration depths from a few micrometers to centimeters [1–9]. OAT exploits the following thermalacoustic effect: when the tissue is illuminated by a short-pulse laser, the absorbed photon energy is converted into ultrasonic waves [1]. Therefore, OAT benefits at the same time from the excellent contrast of optical excitation and from the large penetration depth of ultrasound detection [4, 10]. OAT has been successfully used in a wide range of preclinical and clinical studies for molecular, anatomical, and functional studies such a blood oxygenation [11–13], skin-cancer screening [14, 15], and breast imaging [16–18]. It has not only access to a rich variety of endogenous contrast agents that enable label-free imaging; its specificity is also further enhanced by the introduction of exogenous agents [4, 19, 20], in particular, genetically encoded protein reporters [21]. Among these reporters, the reversibly switchable optoacoustic proteins (rsOAPs) have emerged as a popular choice because of their special photo-physical property of undergoing a change in their absorption spectrum when illuminated with certain wavelengths [5, 22–26]. This switching is reversible and the proteins are robust to photo-fatigue or photobleaching [27, 28]. Such a property can be combined with tailored illumination schedules to ensure that the signal from the target protein is modulated while the background remains unchanged. This technique allows the weak signals from the targets to be distinguished from the strongly-absorbing tissue background and greatly improves the contrast-to-noise ratio [5, 22, 23, 29].

Several techniques have been developed to analyze time series of the OA images of rsOAPs. Differential imaging has been among the first methods being proposed [30]. It is based on a subtraction between OFF- and ON- images, but its exploitation of the switching dynamics is such that it cannot account for multiple reporters. This approach has been extended for two species under the condition of non-overlapping spectra [27], which is still restrictive in practice. More recent studies [23, 28] have proposed to unmix multiple reporters through strategies that include

Fourier analysis, exponential fitting, or classification. These methods proceed pixel-wise and do not exploit any spatial consistency to improve the reconstruction quality in low-SNR settings.

To the best of our knowledge, no quantitative approach exists yet that would directly model the concentration maps of reporters during photoswitching. For instance, what role does the light fluence play during the decay process? In which precise way are the reporters entangled? How can we reconstruct the concentration maps for a species of reporters while taking into account the influence of neighboring pixels? In this paper, we aim to answer these questions. Our contribution is twofold. We detail an accurate mathematical model that explicitly describes the dynamics of the OFF-switching process. Then, we formulate the unmixing as an optimization problem with tailored spatial regularization that encourages smoothness within the targets and reduces noise in the reconstruction. A dedicated algorithm is deployed to solve the optimization problem and recover the concentration maps of multiple species of photoswitchable reporters. Our unmixing method improves upon pixel-wise reconstruction and produces spatially coherent images robust to measurement noise.

## 2. Methods

During a photoswitching experiment, the sample is repeatedly illuminated by a pulsed laser, first at the wavelength  $\lambda_{\text{ON}}$  to switch the proteins on. Then, a sequence of  $N_{\text{pulse}}^{\text{OFF}}$  pulses at the OFF-switching wavelength  $\lambda_{\text{OFF}}$  progressively decreases the intensities of the OA signal of the photoswitchable reporters. This sequence results in a local intensity evolution that is well described by a decaying exponential. Such a process is referred to as an OFF-switching cycle. Afterwards, a cycle of  $N_{\text{pulse}}^{\text{ON}}$  ON-switching pulses at wavelength  $\lambda_{\text{ON}}$  is applied to revert the intensity of the population of reporters to their initial state. This alternation of OFF and ON cycles is repeated  $N_{\text{cycle}}$  times. The background signal ideally remains constant during this modulation process and is usually much stronger due to endogenous absorption of hemoglobin and lipids [5]. The principle of photoswitching OAT is summarized in Fig. 1.

In principle, both the ON- and OFF- switching cycles can be used for unmixing. However, the

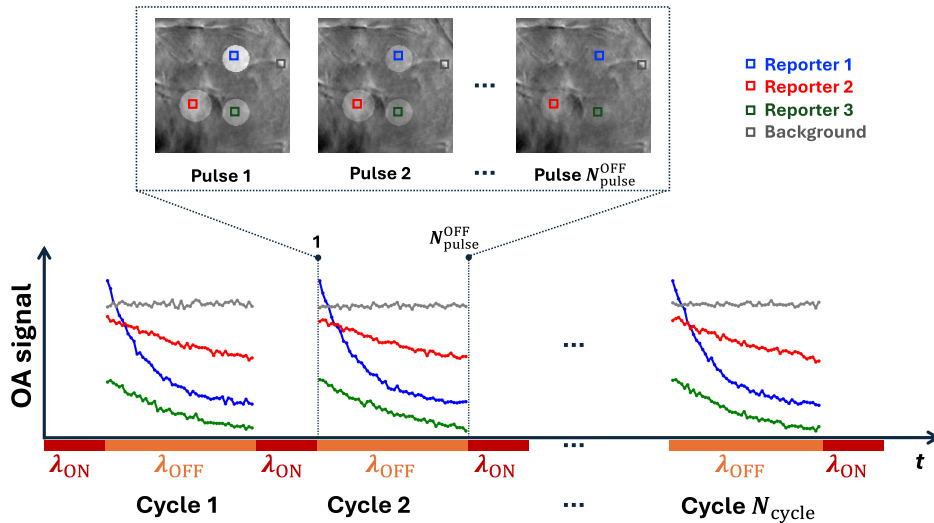


Fig. 1. Principle of reversible photoswitching OAT. Top: Simulated measurement data. Bottom: OA signal at the highlighted locations (three inside reporters in color and one in the background in gray).

OFF-switching cycles are often preferred because they are slower, red-shifted, and have a higher dynamic range for all the photoswitchable proteins used so far [31]. These properties ease the analysis and allow for a larger imaging depth. Accordingly, we present a model that characterizes the decay of OA signals during an OFF-switching cycle of photoswitchable proteins.

### 2.1. Forward Model

We consider  $P$  species of reporters. We assume that the light pulses are independent from each other and that there is no overlap with neighboring switching events. The distribution  $H(\mathbf{r}, t)$  of absorbed optical energy at spatial location  $\mathbf{r}$  and time  $t$  is related to the distribution  $\Phi(\mathbf{r}, t)$  of light fluence and to the concentration map  $c_p$  of each reporter according to

$$H(\mathbf{r}, t) = \Phi(\mathbf{r}, t) \sum_{p=1}^P \varepsilon_p(\mathbf{r}, t) c_p(\mathbf{r}), \quad \mathbf{r} \in \Omega \subset \mathbb{R}^2 \text{ or } \mathbb{R}^3, \quad t \geq 0, \quad (1)$$

where  $\Omega$  is a 2D or 3D spatial domain that represents the sample to be imaged,  $\varepsilon_p(\mathbf{r}, t)$  is the molar extinction coefficient of the  $p$ th reporter. The decay of  $\varepsilon_p(\mathbf{r}, t)$  is exponential during the OFF switching process. It depends on both the light fluence  $\Phi(\mathbf{r}, t)$  and the intrinsic kinetic constant  $k_p$  of the reporter and is modeled as

$$\varepsilon_p(\mathbf{r}, t) = \varepsilon_p^0 e^{-k_p \Phi(\mathbf{r}, t) t}, \quad (2)$$

where  $\varepsilon_p^0$  is the initial extinction coefficient at the OFF-switching wavelength. The combination of Eq. (2) and Eq. (1) yields the forward model

$$H(\mathbf{r}, t) = \Phi(\mathbf{r}, t) \sum_{p=1}^P \varepsilon_p^0 e^{-k_p \Phi(\mathbf{r}, t) t} c_p(\mathbf{r}). \quad (3)$$

In Eq. (3), the unknown quantities are the concentration maps  $c_p(\mathbf{r})$  of the  $P$  species of reporters and the distribution  $\Phi(\mathbf{r}, t)$  of the light fluence within the sample at time  $t$ . We assume that the fluence is constant both over space and time, so that  $\Phi(\mathbf{r}, t) = \Phi_0$ . The assumption that fluence is constant over time is mild because time-dependent absorption due to rsOAPs is orders of magnitude lower than the background signal from indogenous absorbers. However, for large 3D samples or localized-illumination geometries, fluence may vary spatially. In such cases, the spatial distribution of fluence can be estimated through the diffusion equation [32, 33]. Here, we assume a spatially independent fluence owing to the fact that the illumination in our OAT system is wide-field.

Eq. (3) provides the continuous forward model of photoswitching photoacoustic tomography. It relates the measured OA signal  $H$  to the unknown concentration  $c_p$  of the  $p$ th reporter at location  $\mathbf{r}$  and time  $t$ . The series of 2D optical energy deposition maps  $H$  can be derived from the acoustically reconstructed 2D OA images  $p^0$  at the corresponding pulse number via the linear relationship  $p^0 = \Gamma H$ , where  $\Gamma$  is the dimensionless Grüneisen parameter that represents the conversion rate from heat to the initial rise in pressure.

We then proceed to discretize Eq. (3). For the sake of simplicity, we assume in our derivation that the sample is 2D while keeping in mind that the procedure is directly transferable to 3D. We sample the 2D domain  $\Omega$  at the pixel positions  $\mathbf{r} = \mathbf{r}_{i,j}$  and time points (pulses)  $t = t^0, t^1, \dots, t^{N-1}$ . Defining the discrete energy deposition  $h_{ij}^n = h(\mathbf{r}_{i,j}, t^n)$ , reporter concentrations  $c_{p,ij} = c_p(\mathbf{r}_{i,j})$ , and fluence distribution  $\hat{\Phi}_{ij} = \hat{\Phi}(\mathbf{r}_{i,j})$ , the linear system for a pixel  $(i, j)$  is

$$\underbrace{\begin{bmatrix} h_{ij}^0 \\ h_{ij}^1 \\ \vdots \\ h_{ij}^{N-1} \end{bmatrix}}_{\mathbf{H}_{i,j}} = \hat{\Phi}_{i,j} \underbrace{\begin{bmatrix} \varepsilon_1^0 e^{-k_1 \Phi_{i,j} t^0} & \varepsilon_2^0 e^{-k_2 \Phi_{i,j} t^0} & \dots & \varepsilon_P^0 e^{-k_P \Phi_{i,j} t^0} \\ \varepsilon_1^0 e^{-k_1 \Phi_{i,j} t^1} & \varepsilon_2^0 e^{-k_2 \Phi_{i,j} t^1} & \dots & \varepsilon_P^0 e^{-k_P \Phi_{i,j} t^1} \\ \vdots & \vdots & \ddots & \vdots \\ \varepsilon_1^0 e^{-k_1 \Phi_{i,j} t^{N-1}} & \varepsilon_2^0 e^{-k_2 \Phi_{i,j} t^{N-1}} & \dots & \varepsilon_P^0 e^{-k_P \Phi_{i,j} t^{N-1}} \end{bmatrix}}_{\mathbf{S}_{i,j}} \underbrace{\begin{bmatrix} c_{1,i,j} \\ c_{2,i,j} \\ \vdots \\ c_{P,i,j} \end{bmatrix}}_{\mathbf{C}_{i,j}}, \quad (4)$$

where  $\mathbf{H}_{i,j} \in \mathbb{R}^N$ ,  $\mathbf{C}_{i,j} \in \mathbb{R}^P$ , and  $\mathbf{S}_{i,j} \in \mathbb{R}^{N \times P}$ . For a 2D image with  $(L_x L_y)$  pixels, the per-pixel systems Eq. (4) are assembled into a block-diagonal system  $\mathbf{H} = \mathbf{S}\mathbf{C}$  by combining  $L = L_x \times L_y$  systems sequentially as

$$\underbrace{\begin{bmatrix} \mathbf{H}_{0,0} \\ \mathbf{H}_{1,0} \\ \vdots \\ \mathbf{H}_{L_x,0} \\ \mathbf{H}_{0,1} \\ \vdots \\ \mathbf{H}_{L_x,L_y} \end{bmatrix}}_{\mathbf{H}} = \underbrace{\begin{bmatrix} \mathbf{S}_{0,0} & \mathbf{0} & \dots & \dots & \dots & \dots & \mathbf{0} \\ \mathbf{0} & \mathbf{S}_{1,0} & \ddots & \dots & \dots & \dots & \vdots \\ \vdots & \ddots & \ddots & \mathbf{0} & \dots & \dots & \vdots \\ \vdots & \dots & \mathbf{0} & \mathbf{S}_{L_x,0} & \mathbf{0} & \dots & \vdots \\ \vdots & \dots & \dots & \mathbf{0} & \mathbf{S}_{0,1} & \ddots & \vdots \\ \vdots & \dots & \dots & \dots & \ddots & \ddots & \mathbf{0} \\ \mathbf{0} & \dots & \dots & \dots & \dots & \mathbf{0} & \mathbf{S}_{L_x,L_y} \end{bmatrix}}_{\mathbf{S}} \underbrace{\begin{bmatrix} \mathbf{C}_{0,0} \\ \mathbf{C}_{1,0} \\ \vdots \\ \mathbf{C}_{L_x,0} \\ \mathbf{C}_{0,1} \\ \vdots \\ \mathbf{C}_{L_x,L_y} \end{bmatrix}}_{\mathbf{C}}, \quad (5)$$

where  $\mathbf{H} \in \mathbb{R}^{NL}$ ,  $\mathbf{C} \in \mathbb{R}^{PL}$ , and  $\mathbf{S} \in \mathbb{R}^{NL \times PL}$ .

The solution to the unmixing problem recovers individual maps  $\hat{c}_p(\mathbf{r}_{i,j})$  of the concentration of reporters from measurements of the optical deposition  $h(\mathbf{r}_{i,j}, t^n)$  over time via the linear system Eq. (5). In a typical photoswitching OAT experiment, one may have a sample of size  $(20\text{mm} \times 20\text{mm} \times 10\text{mm})$  imaged at an average spatial resolution of  $200\mu\text{m}$ , an OFF-switching window of 5s with a laser repetition rate of 50Hz, and 2 to 5 reporters present. In that case, we have  $N \sim 10^2$ ,  $P \sim 10^0$ , and  $L = L_x L_y \sim 10^4$ , which yields in a linear system of size  $\sim 10^{10}$ . Direct inversion of such a large sparse linear system is computationally challenging and non-robust against measurement noise. We thus adopt a model-based approach instead.

## 2.2. Inverse Problem and Unmixing Algorithm

We retrieve the solution to Eq. (5) by formulating the reconstruction of maps  $\hat{\mathbf{C}}$  as the optimization problem

$$\hat{\mathbf{C}} = \underset{\mathbf{C} \geq 0}{\operatorname{argmin}} J(\mathbf{C}) = \underset{\mathbf{C} \geq 0}{\operatorname{argmin}} \left\{ \frac{1}{2} \|\mathbf{H} - \mathbf{S}\mathbf{C}\|_2^2 + \mathcal{R}(\mathbf{C}) \right\}. \quad (6)$$

The first term of the sum in Eq. (6), commonly called the data-fidelity term, encourages a close fit to the measurement data  $\mathbf{H}$ . The functional  $\mathcal{R}(\mathbf{C})$  in Eq. (6) is called the regularization term. It ensures that the solution is robust to noise and allows us to incorporate some prior information into the solution. Here, we choose  $\mathcal{R}(\mathbf{C})$  to be the combination of total-variation (TV) and  $\ell_1$  regularizers given by

$$\mathcal{R}(\mathbf{C}) = \sum_{p=1}^P \left( \lambda_p^{\text{TV}} |\mathbf{C}_p|_{\text{TV}} + \lambda_p^{\ell_1} \sum_{i,j} \|\mathbf{C}_{i,j}\|_{\ell_1} \right), \quad (7)$$

where  $\mathbf{C}_p \in \mathbb{R}^{L_x \times L_y}$  is the discrete 2D concentration map of the  $p$ th reporter,  $\lambda_p^{\text{TV}} > 0$  and  $\lambda_p^{\ell_1} > 0$  are the TV and  $\ell_1$  regularization weights for the  $p$ th reporter. We choose  $|\mathbf{C}|_{\text{TV}} := \|\nabla_x \mathbf{C}\|_{\ell_1} + \|\nabla_y \mathbf{C}\|_{\ell_1}$ , the anisotropic TV regularizer, for computational efficiency. TV regularization promotes sparsity in the gradient domain to achieve piecewise-smooth reconstructions [34, 35]. The  $\ell_1$  regularization minimizes cross-talk between different species. Through fine-tuning of a combination of the  $(2P)$  hyperparameters  $\{\lambda_p^{\text{TV}}, \lambda_p^{\ell_1}\}_{p=1}^P$ , we achieve a noise-free precise reconstruction of  $P$  maps of the concentration of reporters.

The minimization problem in Eq. (6), combined with the proposed regularization in Eq. (7), is a large-scale nonlinear (due to the non-negativity constraint and regularization) convex problem. For computational speed, we use the limited-memory Broyden–Fletcher–Goldfarb–Shanno (BFGS) algorithm with bound constraints (L-BFGS-B [36]). The forward matrices  $\mathbf{S}_{i,j}$  are constructed efficiently using Einstein summation and assembled into the final system matrix  $\mathbf{S}$  in the form of a linear operator. Finally, the whole pipeline, including the forward operator and the inverse-problem solver, is implemented using *PyLops*, an open-source Python library for large-scale optimization with linear operators [37].

### 3. Results

We first validate the correctness of our proposed algorithm on a simulated phantom of beads. Then, we show the unmixing performance of our algorithm on two experimental datasets of a phantom of beads and a mouse model. Three species of rsOAPs: *ReBphP*-PCM (Re), *DrBphP*-PCM (Dr), and *RpBphP1*-PCM (Rp) are used throughout Section 3. We provide in Table 1 in Appendix A the photo-physical properties relevant to the analysis in this paper and refer the reader to [28] for more details on the reporters.

#### 3.1. Validation on Synthetic Data

We design a 2D numerical phantom of size  $(150 \times 150)$ px in which we randomly insert three groups of disk-like objects of diameter between 7px and 12px on a heterogeneous background. The background image is taken from an image (cropped to contain only areas of the sample) of the last pulse of the first OFF-switching cycle from the experimental dataset of the mouse model. Each disk-like object mimics a bead with homogeneous intensity. The ratio of the initial intensities between the three groups and the maximum intensity of the background is 2:1:1:5, meaning that the background signal is considerably higher than that of the reporters. Each group has the same kinetic constant as one of the three rsOAPs used in the experiment. The forward model Eq. (5) is used to generate measurements of a set of a total of 100 2D OA switching images of size  $(150 \times 150)$ px. A level of 1% Gaussian white noise is added to the simulated measurements to mimic to the noise level in the experimental datasets (see Appendix A Fig. 4 for details).

We tested three reconstruction approaches, namely, least-square only (LS), least-square regularized with total variation on the spatial maps of each reporter (LS+TV), and least-square regularized with TV and additionally  $\ell_1$  among the reporters (LS+TV+ $\ell_1$ ). We compare in Fig. 2 the results of using these methods against the ground truth. In all the scenarios, the three groups of reporters are successfully extracted from the non-switching background which is well recovered with a perfect structural similarity index (SSIM) of 1.0, though the peak signal-to-noise ratio (PSNR) varies among different methods.

Without any regularization, the unmixing performs well only on the first group of reporters, which has the largest kinetic constant, achieving an SSIM of 0.9 out of 1. However, the algorithm struggles to separate the second and the third groups. This is indicated by the presence of reporters belonging to the third group appearing in the map of the second, leading to an SSIM of only 0.79 for the second group.

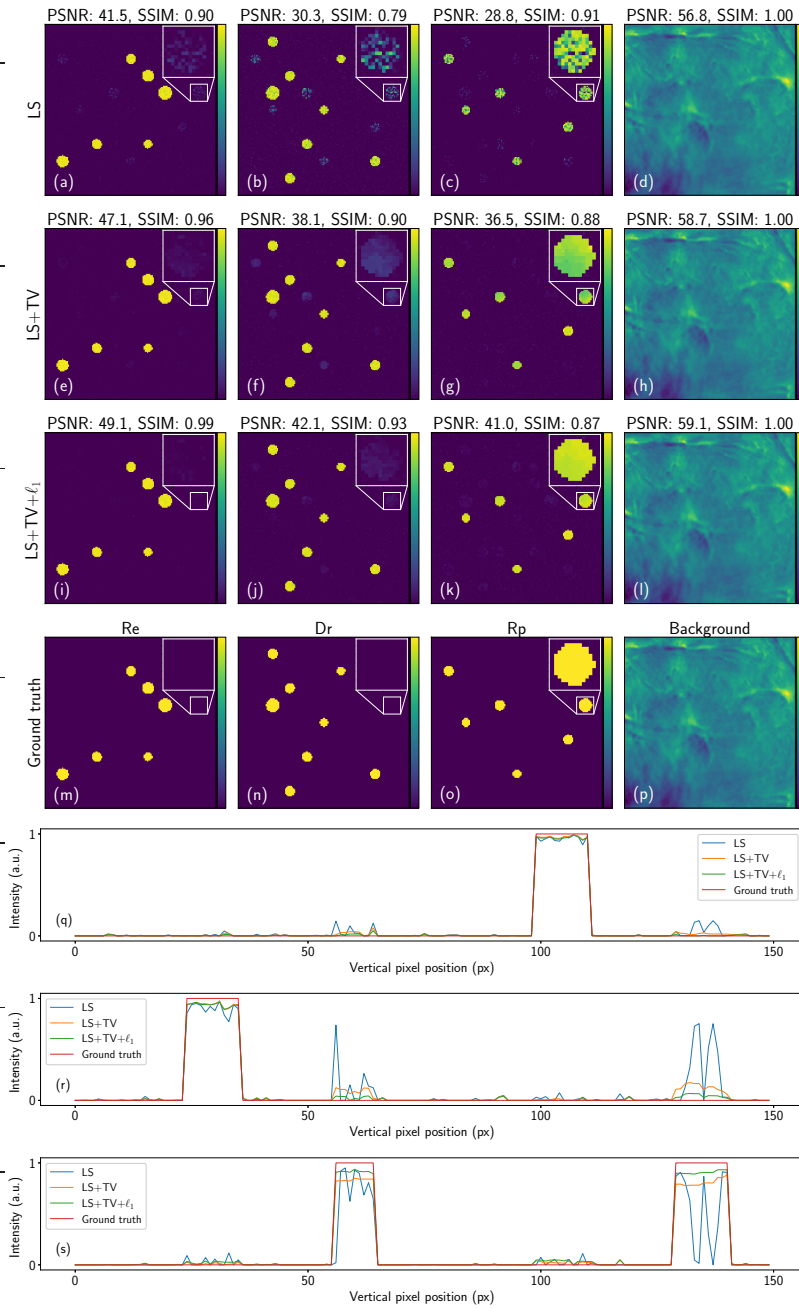


Fig. 2. Unmixing results of a simulated phantom of beads mimicking the experimental phantom. The first three rows each contains reconstructed distribution maps of the three rsOAPs shown in column one to three and the non-switching background image in the last column. The PSNR and SSIM of each reconstruction is indicated on top of each image. Row one (a)-(d): least-square solution. Row two (e)-(h): least-square with total variation regularization. Row three (i)-(l): least-square with total variation and  $\ell_1$  regularization. Row four (m)-(p): ground truth. (q)-(s): horizontal intensity profiles at the 60th row of pixels of the reporter Re (q), Dr (r), and Rp (s) for each reconstruction method. The intensities of all images are normalized to  $[0, 1]$  for visual comparison.

In fact, reporters of the third group “bleed” into the maps of the first two groups (see the zoomed-in area in Fig.2 (a) and (b)). After having added a TV regularizer for each group and tuned the regularization weights, we observe in Fig. 2 (e)-(g) that TV not only reduces noise inside the beads, giving a much smoother intensity distribution for each of them, but also greatly mitigates the bleed-through issue if we compare Fig. 2 (b) and (f). The PSNR of each group enjoys an average boost of 7dB due to the noise reduction and the SSIM of reporters Re and Dr is improved by 7% on average. However, there is still a hint of a remaining bleed-through in Fig. 2 (f), which is solved by the further addition of an  $\ell_1$  regularizer to enforce sparsity at each pixel. This proves to effectively solve the bleed-through problem and the intensity of each bead is more uniform, increasing the PSNR of each map by another 2-5dB (see Fig. 2 (i)-(k)).

To gain more insight on the reconstruction quality, we compare the intensity profiles along a representative horizontal line at the 60th row in Fig. 2 (q)-(s). We see that LS+TV+ $\ell_1$  outperforms LS only and LS+TV in the sense that, on one hand, the signal is correctly recovered at nearly its 100% intensity with very little fluctuation inside the bead (see signals at location 55px and 140px in Fig. 2 (s) for a good example) and that, on the other hand, LS+TV+ $\ell_1$  does not suffer from the bleed-through issue on locations where there should not be any signal compared to the other two approaches. Taking the signals at location 55px and 140px in Fig. 2 (q) and (r) as an example, LS only and LS+TV show relatively prominent peaks at these two locations where the signals from the third group should not appear at all, while LS+TV+ $\ell_1$  shows only flat tiny bumps. Hence, we conclude that our proposed reconstruction method, which combines TV and  $\ell_1$  regularization with least square, yields the best reconstruction results. The code to reproduce the simulation results is available in [38].

### 3.2. Validation on Real Data

We validated our proposal on a physical phantom of beads and on a mouse model, imaged with a commercially available MSOT scanner [28]. The phantom contains 1mm-alginate beads inserted at random locations. Each bead contains *E. coli* that express one of the three rsOAPs: Re, Dr, and Rp. In the case of the mouse model, Jurkat T cells and *E. coli* expressing each of the three rsOAPs are implanted into a 4T1 tumor on the back of a mouse in the same plane. We kindly refer the reader to [28] for details on sample preparation, data acquisition, and instrumental setup.

The experimental phantom datasets contain 2D OA images of size  $(300 \times 300)$ px of 50 OFF-switching pulses averaged over 50 OFF-switching cycles to reduce detection noise. Further, only the first 25 pulses of the experimental phantom datasets are used for unmixing as dynamics are dominated by noise fluctuations afterwards (see Appendix A Fig. 4 (b) for details). The mouse dataset of 25 OFF-switching pulses averaged over 50 cycles contains 2D OA images that are cropped from  $(332 \times 332)$ px down to  $(120 \times 90)$ px to minimize the area devoid of switching information and thus reduce computational time.

To build the forward matrix  $\mathbf{S}$  for the experimental dataset, the knowledge of the distribution of the light fluence and the intrinsic kinetic constants  $k_p$  is required. We set the fluence distribution as a constant  $\Phi_0$  over space and time. The kinetic constants  $k_p$  are first calculated from the measured OFF-switching half-time values (see Appendix A, Table 1), then tuned based on an empirical analysis of the experimental dataset (see Appendix B for details).

We show in Fig. 3 (a)-(h) that our unmixing algorithm successfully reconstructs the quantitative spatial distribution of the three rsOAPs both for the beads phantom and for the mouse model. Our results agree with the classification results from [28] and we can correctly separate the three groups of reporters as well as the background. Compared to qualitative classification, our approach is able to obtain the quantitative concentration maps of different reporters.

The overlay images of Fig. 3 allow us to compare the results of our proposed approach (Fig. 3 (j) and (l)) against those of the unregularized approach (Fig. 3 (i) and (k)). We observe that,

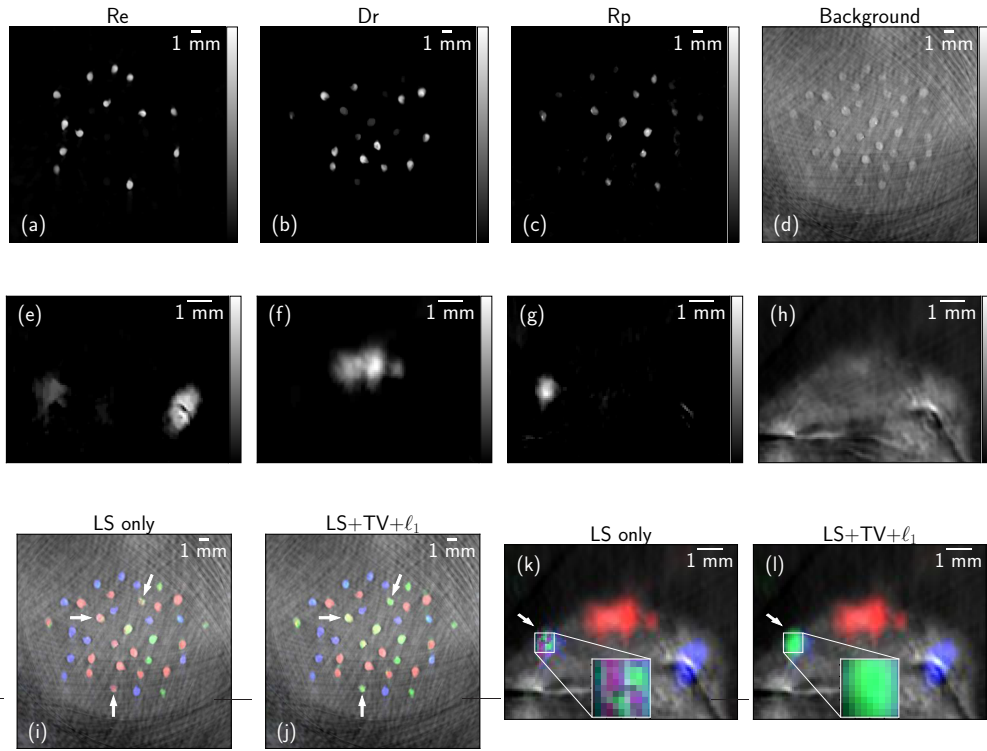


Fig. 3. Quantitative unmixing results of a phantom of beads and mouse model. First two rows (a)-(h): reconstructed concentration maps of rsOAPs Re ((a) and (e)), Dr ((b) and (f)), and Rp ((c) and (g)) using the proposed combination of TV and  $\ell_1$  regularization. (d) and (h): background. The color images (i)-(l) visualize the maps of the three reconstructed rsOAPs overlaid on the background (produced using Fiji [39]). Re, Dr and Rp are represented by blue, red, and green channels. The background is grayscale. Color images (i) and (k) represent the reconstruction result without any regularization; (j) and (l) represent the result with our proposed regularization method. The arrows in (i) point out some of the beads belonging to the species Rp that were unsuccessfully unmixed under unregularized reconstruction compared to the successful outcome with regularization in (j). We provide a zoom-in of the details of the unmixing results of Rp in (k) and (l) to ease the comparison of the unregularized and regularized methods. The intensities of all the images are normalized to [0, 1] for cross-comparison and color visualization.

without any regularization, some beads belonging to the Rp channel show up in the Dr channel for instance those pointed out by the arrows in Fig. 3 (i) and (j). The effect of regularization is even more obvious when we zoom in onto the Rp species in the reconstruction result of the mouse images in Fig. 3 (k) and (l). In the absence of regularization, the Rp reporter cannot be properly unmixed from the other two, as indicated by the zoom-in region in Fig. 3 (k). With our proposed regularization, the same region is cleanly unmixed with coherent intensity distribution, as observed in Fig. 3 (l).

#### 4. Conclusion and Discussion

We presented a quantitative unmixing framework to reconstruct the concentration maps of multiple species of photoswitching reporters using optoacoustic tomography. This framework is

based on a mathematical model that describes how the time-series of OA images decays during the OFF-switching process. Our model explicitly relates the unknown concentration maps to the factors that govern the switching dynamics, namely, the reporter kinetic constant, the extinction coefficient, and the distribution of light fluence in the sample. We make the best use of the full time-series information during OFF-switching cycles on the whole image, thus avoiding the shortcomings of pixel-wise analysis. This also enables the addition of carefully designed spatial regularization to the inverse reconstruction problem. The combination of total variation and  $\ell_1$  regularizers helps reduce noise and improves the separation of different species of reporters, which is crucial to a successful unmixing and high-quality reconstruction of images.

The proposed framework offers quantitative analysis of the temporally entangled OA data during photoswitching experiments. This approach is versatile and easily applicable to various geometries such as 2D cross-sectional images or 3D volumes acquired with a raster-scanning or tomographic OA setup. Our framework also allows for a realistic map of the heterogeneous light fluence distribution, which can be separately estimated with another model, to be conveniently incorporated in the forward model for high-quality volume unmixing.

**Funding.** This project was funded by the European Union's Horizon Europe research and innovation programme under Grant Agreement No. 101046667 (SWOPT).

**Acknowledgments.** We would like to thank Eric Sinner for his help in the code base.

**Disclosures.** The authors declare no conflicts of interest.

**Data availability.** Data underlying the results presented in this paper are not publicly available at this time but may be obtained from the authors upon reasonable request.

## References

1. L. V. Wang and S. Hu, "Photoacoustic Tomography: In Vivo Imaging from Organelles to Organs," *Science* **335**, 1458–1462 (2012).
2. J. Yao and L. V. Wang, "Sensitivity of photoacoustic microscopy," *Photoacoustics* **2**, 87–101 (2014).
3. A. Taruttis and V. Ntziachristos, "Advances in real-time multispectral optoacoustic imaging and its applications," *Nat. Photonics* **9**, 219–227 (2015).
4. L. V. Wang and J. Yao, "A practical guide to photoacoustic tomography in the life sciences," *Nat. Methods* **13**, 627–638 (2016).
5. J. Yao, J. Xia, and L. V. Wang, "Multiscale Functional and Molecular Photoacoustic Tomography," *Ultrason. Imaging* **38**, 44–62 (2016).
6. T. Vu, D. Razansky, and J. Yao, "Listening to tissues with new light: recent technological advances in photoacoustic imaging," *J. Opt.* **21**, 103001 (2019).
7. X. L. Deán-Ben and D. Razansky, "Optoacoustic image formation approaches—a clinical perspective," *Phys. Med. & Biol.* **64**, 18TR01 (2019).
8. M. Omar, J. Aguirre, and V. Ntziachristos, "Optoacoustic mesoscopy for biomedicine," *Nat. Biomed. Eng.* **3**, 354–370 (2019).
9. J. Yao and L. V. Wang, "Perspective on fast-evolving photoacoustic tomography," *J. Biomed. Opt.* **26** (2021).
10. V. Ntziachristos, "Going deeper than microscopy: the optical imaging frontier in biology," *Nat. Methods* **7**, 603–614 (2010).
11. X. Wang, X. Xie, G. Ku, *et al.*, "Noninvasive imaging of hemoglobin concentration and oxygenation in the rat brain using high-resolution photoacoustic tomography," *J. biomedical optics* **11**, 024015–024015 (2006).
12. M. Li, Y. Tang, and J. Yao, "Photoacoustic tomography of blood oxygenation: A mini review," *Photoacoustics* **10**, 65–73 (2018).
13. M. Tomaszewski, I. Quiros Gonzalez, J. O'Connor, *et al.*, "Oxygen enhanced optoacoustic tomography (oe-ot) reveals vascular dynamics in murine models of prostate cancer," *Theranostics* **7**, 2900–2913 (2017).
14. I. Stoffels, S. Morscher, I. Helfrich, *et al.*, "Metastatic status of sentinel lymph nodes in melanoma determined noninvasively with multispectral optoacoustic imaging," *Sci. translational medicine* **7**, 317ra199–317ra199 (2015).
15. H. He, C. Schönmann, M. Schwarz, *et al.*, "Fast raster-scan optoacoustic mesoscopy enables assessment of human melanoma microvasculature in vivo," *Nat. Commun.* **13**, 2803 (2022).
16. S. A. Ermilov, T. Khamapirad, A. Conjusteau, *et al.*, "Laser optoacoustic imaging system for detection of breast cancer," *J. biomedical optics* **14**, 024007–024007 (2009).
17. G. Diot, S. Metz, A. Noske, *et al.*, "Multispectral optoacoustic tomography (msot) of human breast cancer," *Clin. Cancer Res.* **23**, 6912–6922 (2017).

18. X. Li, C. D. Heldermon, L. Yao, *et al.*, “High resolution functional photoacoustic tomography of breast cancer,” *Med. physics* **42**, 5321–5328 (2015).
19. G. P. Luke, D. Yeager, and S. Y. Emelianov, “Biomedical applications of photoacoustic imaging with exogenous contrast agents,” *Ann. biomedical engineering* **40**, 422–437 (2012).
20. Y. Wang, X. Xie, X. Wang, *et al.*, “Photoacoustic tomography of a nanoshell contrast agent in the in vivo rat brain,” *Nano letters* **4**, 1689–1692 (2004).
21. J. Brunker, J. Yao, J. Laufer, and S. E. Bohndiek, “Photoacoustic imaging using genetically encoded reporters: a review,” *J. Biomed. Opt.* **22**, 070901 (2017).
22. A. C. Stiel, X. L. Deán-Ben, Y. Jiang, *et al.*, “High-contrast imaging of reversibly switchable fluorescent proteins via temporally unmixed multispectral optoacoustic tomography,” *Opt. Lett.* **40**, 367 (2015).
23. L. Li, A. A. Shemetov, M. Baloban, *et al.*, “Small near-infrared photochromic protein for photoacoustic multi-contrast imaging and detection of protein interactions in vivo,” *Nat. Commun.* **9**, 2734 (2018).
24. K. Mishra, J. P. Fuenzalida-Werner, V. Ntziachristos, and A. C. Stiel, “Photocontrollable Proteins for Optoacoustic Imaging,” *Anal. Chem.* **91**, 5470–5477 (2019).
25. K. Mishra, J. P. Fuenzalida-Werner, F. Pennacchietti, *et al.*, “Genetically encoded photo-switchable molecular sensors for optoacoustic and super-resolution imaging,” *Nat. Biotechnol.* (2021).
26. L. Li, H. Hsu, V. V. Verkhusa, *et al.*, “Multiscale Photoacoustic Tomography of a Genetically Encoded Near-Infrared FRET Biosensor,” *Adv. Sci.* p. 2102474 (2021).
27. R. K. W. Chee, Y. Li, W. Zhang, *et al.*, “In vivo photoacoustic difference-spectra imaging of bacteria using photoswitchable chromoproteins,” *J. Biomed. Opt.* **23**, 106006 (2018).
28. K. Mishra, M. Stankevych, J. P. Fuenzalida-Werner, *et al.*, “Multiplexed whole-animal imaging with reversibly switchable optoacoustic proteins,” *Sci. Adv.* **6**, eaaz6293 (2020).
29. X. L. Deán-Ben, A. C. Stiel, Y. Jiang, *et al.*, “Light fluence normalization in turbid tissues via temporally unmixed multispectral optoacoustic tomography,” *Opt. Lett.* **40**, 4691 (2015).
30. J. Yao, A. Kaberniuk, L. Li, *et al.*, “Multiscale photoacoustic tomography using reversibly switchable bacterial phytochrome as a near-infrared photochromic probe,” *Nat. methods* **13**, 67–73 (2016).
31. M. Stankevych, K. Mishra, V. Ntziachristos, and A. C. Stiel, “A practical guide to photoswitching optoacoustics tomography,” in *Methods in Enzymology*, vol. 657 (Elsevier, 2021), pp. 365–383.
32. A. Q. Bauer, R. E. Nothdurft, T. N. Erpelding, *et al.*, “Quantitative photoacoustic imaging: correcting for heterogeneous light fluence distributions using diffuse optical tomography,” *J. Biomed. Opt.* **16**, 096016 (2011).
33. B. Cox, J. G. Laufer, S. R. Arridge, and P. C. Beard, “Quantitative spectroscopic photoacoustic imaging: a review,” *J. Biomed. Opt.* **17**, 061202 (2012).
34. A. Chambolle, “An Algorithm for Total Variation Minimization and Applications,” *J. Math. Imaging Vis.* **20**, 89–97 (2004).
35. M. Unser, J. Fageot, and H. Gupta, “Representer theorems for sparsity-promoting l1 regularization,” *IEEE Trans. on Inf. Theory* **62**, 5167–5180 (2016).
36. R. H. Byrd, P. Lu, J. Nocedal, and C. Zhu, “A limited memory algorithm for bound constrained optimization,” *SIAM J. on Sci. Comput.* **16**, 1190–1208 (1995).
37. M. Ravasi and I. Vasconcelos, “Pylops—a linear-operator python library for scalable algebra and optimization,” *SoftwareX* **11**, 100361 (2020).
38. <https://doi.org/10.5281/zenodo.11148506>.
39. J. Schindelin, I. Arganda-Carreras, E. Frise, *et al.*, “Fiji: an open-source platform for biological-image analysis,” *Nat. Methods* **9**, 676–682 (2012).

## A. Supporting Tables and Figures

We provide an extract of the key photo-physical properties of the reversibly switchable OA reporters (rsOAPs) used in the experiments in Table 1. For a complete summary of the full properties of these reporters, refer to [28].

Name	$\tau_{\text{OFF}}$ (s)	$\bar{k}$ ( $\text{s}^{-1}$ )	$\varepsilon_{\text{ON}}^0$ ( $\text{mol}^{-1} \text{cm}^{-1}$ )	$\varepsilon_{\text{OFF}}^0$ ( $\text{mol}^{-1} \text{cm}^{-1}$ )
<i>Re</i> BphP-PCM (Re)	0.18	3.85	84520	11272
<i>Dr</i> BphP-PCM (Dr)	0.70	0.99	74812	41197
<i>Rp</i> BphP1-PCM (Rp)	0.42	1.65	78300	87500

Table 1. Key photo-physical properties of the three rsOAPs used in the experiments: half time of the OFF switching cycle  $\tau_{\text{OFF}}$ ; kinetic constant  $\bar{k}$  derived based on  $\tau_{\text{OFF}}$ ; molar extinction coefficients  $\varepsilon_{\text{ON}}^0$ ,  $\varepsilon_{\text{OFF}}^0$  at ON (680nm) and OFF (770nm) wavelengths.

We provide in Fig. 4 a comparison of the OA signal during a typical OFF switching cycle in simulations and experiments of a phantom of beads. The noise level in the simulation is chosen such that the OA signal decay resembles that of the experimental phantom. In (b), we observe that after 25 time steps (marked with a vertical gray dashed line), there is less useful information in the signal other than noise. Hence, only the first 25 frames of OA images are used in the reconstruction.

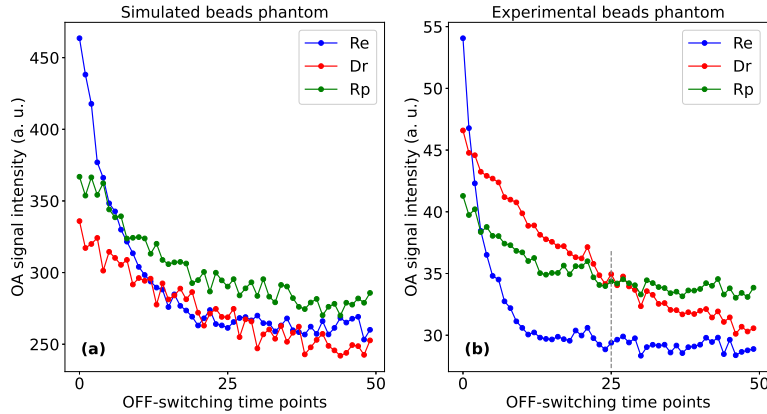


Fig. 4. Evolution of the OA signal during an OFF-switching cycle of 50 time points at three representative locations inside the three rsOAPs: Re (blue), Dr (red), and Rp (green) for the simulated measurements (a) and experimental measurements (b) of a beads phantom. The noise level in the measurements of the simulated beads phantom is 1%.

## B. Estimation of the kinetic constants

The kinetic constants  $\bar{k}$  reported in Table 1 are measured experimentally and depend on the pulse energy and the subsequent unknown light fluence  $\Phi_m$  during the measurement via  $k = \frac{\bar{k}}{\Phi_m}$ , where  $k$  is the intrinsic constant. To estimate  $\Phi_m$ , we first use an empirical method to retrieve the decay rates  $\{b_{\text{Re}}, b_{\text{Dr}}, b_{\text{Rp}}\}$  of each species from the experimental dataset. Then, we determine

$\Phi_m$  from

$$\Phi_m = \sqrt[3]{\frac{\bar{k}_{Re}}{b_{Re}} \frac{\bar{k}_{Dr}}{b_{Dr}} \frac{\bar{k}_{Rp}}{b_{Rp}}}, \quad (8)$$

which is a cubic square root of the estimated results from all three species. To estimate the  $\{b_{Re}, b_{Dr}, b_{Rp}\}$ , we fit an exponential function

$$y = ae^{-bt} + c \quad (9)$$

at each pixel to obtain a map of the decay rates  $b$ . Then, we approximate the OFF-switching rate of each reporter by locating the peaks in the histogram of the map of  $b$ . In Fig. 5(a), we show an example of the fitting result at one location inside each of the three rsOAPs marked by the three dots in Fig. 5(b) for the dataset of the experimental phantom of beads. In Fig. 5(c), we show the result of the empirical estimate of the kinetic constants. Three prominent peaks are observed, indicating the decay rates of the three species. We take a value around these peaks as the empirical estimate for  $\{b_{Re}, b_{Dr}$  and  $b_{Rp}\}$ . Plugging the estimated  $\{b_{Re}, b_{Dr}, b_{Rp}\}$  in Fig. 5 and  $\bar{k}_{Re}, \bar{k}_{Dr}, \bar{k}_{Rp}$  in Table 1 into (B), we obtain that  $\Phi_m = 0.3$ .

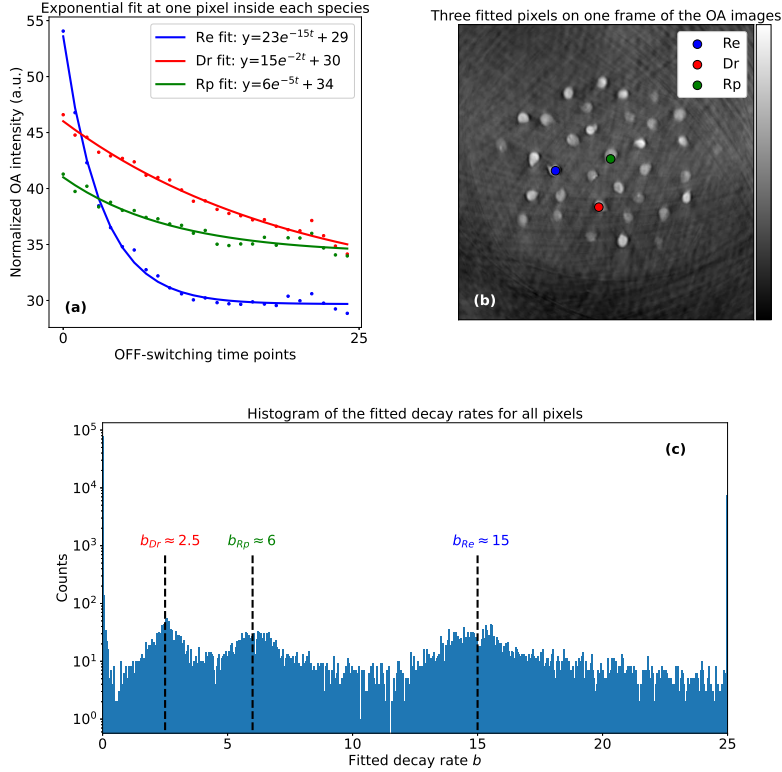


Fig. 5. Estimation of the decay rates for the three species based on the OFF-switching dataset of the experimental phantom of beads. (a) Fitting results at three representative pixels, each inside one of the three rsOAPs. The original data is the scatter points, the curves are the fitted results. (b) Location of the three pixels used in (a). The OA image is the first frame of the OFF-switching series. (c) Histogram (partial) of the fitted decay rate  $b$  for all the pixels in the OA image. Based on the fitting result in (a), only the part of the histogram where the values within the range ( $<25$ ) is displayed.